Concurrent attenuation of, and energy harvesting from, surface vibrations: experimental verification and model validation

2012 Smart Mater. Struct. 21 035016

(http://iopscience.iop.org/0964-1726/21/3/035016)

Smart Mater. Struct. **21** (2012) 035016 (12pp) doi:10.1088/0964-1726/21/3/035016

Concurrent attenuation of, and energy harvesting from, surface vibrations: experimental verification and model validation

Ryan L Harne

Department of Mechanical Engineering, Virginia Polytechnic Institute and State University, 131 Durham Hall (MC 0238), Blacksburg, VA 24061, USA

E-mail: rharne@vt.edu

Received 24 October 2011, in final form 26 January 2012
Published 16 February 2012
Online at stacks.iop.org/SMS/21/035016

Abstract
Fundamental studies in vibrational energy harvesting consider the electromechanically coupled devices to be excited by uniform base vibration. Since many harvester devices are mass–spring systems, there is a clear opportunity to exploit the mechanical resonance in a fashion identical to tuned mass dampers to simultaneously suppress the vibration of the host structure via reactive forces while converting the 'absorbed' vibration into electrical power. This paper presents a general analytical model for the coupled electro-elastic dynamics of a vibrating panel to which distributed energy harvesting devices are attached. One such device is described which employs a corrugated piezoelectric spring layer. The model is validated by comparison to measured elastic and electric frequency response functions. Tests on an excited panel show that the device, contributing 1% additional mass to the structure, concurrently attenuates the lowest panel mode accelerance by >20 dB while generating 0.441 μW for a panel drive acceleration of 3.29 m s^{-2}. Adjustment of the load resistance connected to the piezoelectric spring layer verifies the analogy between the present harvester device and an electromechanically stiffened and damped vibration absorber. The results show that maximum vibration suppression and energy harvesting objectives occur for nearly the same load resistance in the harvester circuit.

(Some figures may appear in colour only in the online journal)

1. Introduction

Vibrational energy harvesting aims to convert ambient vibration into useful electric power by means of novel electromechanical transducers. Mass–spring systems are frequently employed whereby piezoelectric materials may serve as the spring. Such reactive devices are a mainstay in passive vibration control applications since the oscillators work against a host structure or system at a tuned natural frequency.

A typical numerical model in energy harvesting analysis considers the harvester to be excited by the base vibration, neglecting the device's influence on the host structure [1–3]. However, structural dynamic coupling is the foundational assumption in vibration control modeling. The discrepancy exists since early energy harvesting studies considered sources of vibration of massive inertial influence relative to the harvester, for instance bridge vibrations [4, 5] or wireless sensor vibrations having MEMS harvesters [6]. It was therefore reasonably assumed that applying such harvesters to these systems would not influence the dynamics of the host structure.

As material advances are made and practical applications of energy harvesting are demonstrated, there has arisen an interest to convert almost any source of vibrational energy into electrical power. However, some applications involve

vibrating systems which are more likely to be dynamically influenced by applied harvester devices. Therefore, when the attached devices become more inertially substantial relative to the host structure, a new analysis of the coupled electro-elastic dynamics must be considered.

In contrast to the present literature which has rigorously evaluated the electromechanical influences acting on the harvester itself [1, 7–9], this study is concerned with the greater dynamic effects involved between the host exciting structure and the applied harvesters. In this light, energy harvesting devices are analogous to electromechanically stiffened and/or damped vibration absorbers. Thus, the devices suppress the vibration of the exciting structure and convert a portion of the 'absorbed' energy into electrical power. In this capacity, the harvesters have substantially greater mechanical dynamic influence on the host structure than in the prior energy harvesting literature in which the shunt damping effect was exploited simultaneously with harvesting capability [10]. This dual-purpose use of the energy harvesting vibration absorber has recently been investigated in applications for tuned mass dampers of high-rise buildings [11] and a separate scaled experimental study suggested a real-world power output of the order of 100 W with one electromagnetic harvester design [12].

Many of the present successful piezoelectric energy harvesting devices to date have been developed using cantilevered beam designs [8, 13, 14]. The advantage of these embodiments are the large strains induced along the beam as it oscillates in the first mode, which induce the greatest electrical potentials across the piezoceramic electrodes. However, in vibration control applications, cantilever beam vibration absorbers are frequently not employed since they induce bending moments upon the structures to which they are attached [15]. Most vibration control applications require devices to exert reactive forces as opposed to moments in order to work against either the one-dimensional motion of a simple structure or the flexural motion of a vibrating surface.

This paper describes a study of one such device developed for this purpose. The device exhibits a transverse single-degree-of-freedom (SDOF) resonance but is also suitable to attenuate the vibration of surfaces since it employs continuously distributed mass and spring layers. In addition, the spring layer is constructed of a corrugated piezoelectric material such that, as it deforms at the device resonance, it generates a significant electric potential which is then connected to an external energy harvesting circuit. The design of the passive device is similar to the manifestation achieved for actuating purposes by Fuller and Cambou [16] using an etched and circularly corrugated piezoelectric spring layer earlier patented by Tibbetts [17].

A model based on the generalized Hamilton's principle is briefly presented which describes the coupled electro-elastic dynamics of a vibrating rectangular panel to which a number of such distributed piezoelectric vibration control devices are attached. The model is validated by comparison against experimental measurements of a piezoelectric device's elastic and electrical dynamics on a shaker table. An experimental set-up is then described in which a large, lightly damped and simply supported panel is excited by random vibration. A second piezoelectric device is manufactured and applied to this panel to consider its capability to simultaneously suppress the panel vibration and generate electrical power when the piezoelectric electrodes are attached to an external circuit.

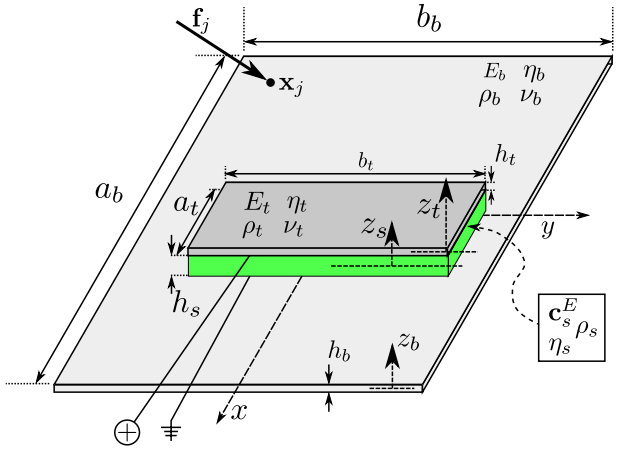

Figure 1. Geometry and material properties of base plate structure with attached piezoelectric vibration control devices.

The model is found to accurately predict the vibration suppression capability of the device as well as the electrical response around the device's SDOF resonance. As observed in other energy harvesting studies [7, 9], changes of the load resistance in the harvester circuit affect the stiffening and damping of the distributed piezoelectric spring layer, which thereafter affect its influence in reactively suppressing the panel vibration. For the lightweight piezoelectric device applied, it is found that the dual objectives are not contradictory and appear to be best met when employing nearly the same load resistance in the harvester circuit.

2. Model description

2.1. Mechanical domain description

Consider a system composed of a base plate to which one or more distributed piezoelectric vibration control devices are attached, figure 1. The attached devices are each composed of a distributed spring layer and a distributed top plate. The spring layer itself is a continuous layer exhibiting piezoelectric characteristics. In the following analysis, subscripts b, s and t refer to the base plate, the continuous spring layer and the distributed top plate, respectively.

The origin of the global coordinate system is defined at the base plate center point and the (x, y) plane corresponds to the base plate mid-plane, $z_b = 0$. The base plate is arbitrarily bounded and may be excited by a number, N_f, of localized point forces, $\mathbf{f}_j(\mathbf{x}_j)$, where $j = 1, 2, \ldots, N_f$ and $\mathbf{x}_j = (x_j, y_j, 0)$.

The base plate and distributed top plate are assumed to be Love–Kirchhoff (LK) plates having displacements expressed

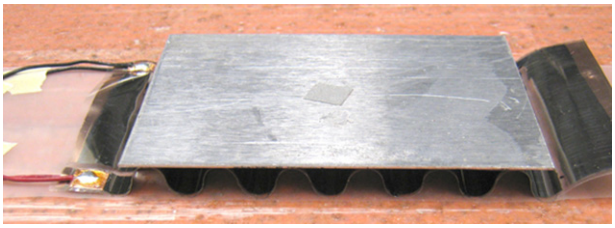

Figure 2. Photograph of piezoelectric vibration control device using a circularly corrugated piezoelectric film as the distributed spring layer. Electrical leads are also shown to be attached to the etched surface electrodes of the film.

in the form

$$\mathbf{u}\,(\mathbf{x},\,t)_{i=\mathrm{b,t}} = \begin{bmatrix} u_{io}(x,\,y,\,t) - z_i \dfrac{\partial w_{io}(x,\,y,\,t)}{\partial x} \\ v_{io}(x,\,y,\,t) - z_i \dfrac{\partial w_{io}(x,\,y,\,t)}{\partial y} \\ w_{io}(x,\,y,\,t) \end{bmatrix} \tag{1}$$

where the second subscript o indicates the displacement in the mid-plane of the plate, $z_\mathrm{b} = 0$ or $z_\mathrm{t} = 0$.

The distributed spring layer is considered to be a thick, transversely deformable, orthotropic plate. Elastic properties of the layer, as described by the stiffness matrix $\mathbf{c}_\mathrm{s}^\mathrm{E}$ evaluated at constant electric field, are assumed to either be known or are able to be computed approximately. The mechanical displacements of the thick orthotropic plate allow for the transverse compressibility of the layer:

$$\mathbf{u}\,(\mathbf{x},\,t)_\mathrm{s} = \begin{bmatrix} u_{so}(x,\,y,\,t) + z_\mathrm{s}\theta_x(x,\,y,\,t) \\ v_{so}(x,\,y,\,t) + z_\mathrm{s}\theta_y(x,\,y,\,t) \\ w_{so}(x,\,y,\,t) + z_\mathrm{s}\dfrac{\partial w_{so}(x,\,y,\,t)}{\partial z_\mathrm{s}} + \dfrac{1}{2}z_\mathrm{s}^2\dfrac{\partial^2 w_{so}(x,\,y,\,t)}{\partial z_\mathrm{s}^2} \end{bmatrix} \tag{2}$$

where θ_x and θ_y are the rotations about the middle planes in the x and y axes, respectively. Application of the continuity of displacements and transverse stress between the spring layer and the two bounding plates allows the spring layer mechanical displacements to be expressed in terms of the top plate and bottom plate displacements:

$$\mathbf{u}(\mathbf{x},\,t)_s = \begin{bmatrix} \left(\dfrac{1}{2}\left[u_{to} + u_{bo}\right] + \dfrac{1}{4}\left[h_t\dfrac{\partial w_{to}}{\partial x} - h_b\dfrac{\partial w_{bo}}{\partial x}\right]\cdots \right. \\ \left. + \dfrac{1}{h_s}z_s\left\{\left[u_{to} - u_{bo}\right] + \dfrac{1}{2}\left[h_t\dfrac{\partial w_{to}}{\partial x} + h_b\dfrac{\partial w_{bo}}{\partial x}\right]\right\}\right) \\ \left(\dfrac{1}{2}\left[v_{to} + v_{bo}\right] + \dfrac{1}{4}\left[h_t\dfrac{\partial w_{to}}{\partial y} - h_b\dfrac{\partial w_{bo}}{\partial y}\right]\cdots \right. \\ \left. + \dfrac{1}{h_s}z_s\left\{\left[v_{to} - v_{bo}\right] + \dfrac{1}{2}\left[h_t\dfrac{\partial w_{to}}{\partial y} + h_b\dfrac{\partial w_{bo}}{\partial y}\right]\right\}\right) \\ \left(\dfrac{1}{2}\left[w_{to} + w_{bo}\right] + \dfrac{1}{h_s}z_s\left[w_{to} - w_{bo}\right]\right) \end{bmatrix} \tag{3}$$

2.2. Electrical domain description

Depending on the specific embodiment of the piezoelectric spring layer under study, one must appropriately select how to include electromechanical coupling effects in the analysis. The present inclusion of piezoelectric material in the spring layer is in the form of a circularly corrugated layer. A photograph of the full device is shown in figure 2 and a diagram of the cross-sectional geometry is given in figure 3(a). As the full vibration control device oscillates transversely at its SDOF natural frequency, bending strain is induced in the corrugated piezoelectric material. However, on a given surface electrode, these strains are out-of-phase from one half-period of the corrugation to the next, figure 3(b). Thus, studies by Gentry-Grace [18] showed that etching of the electrode every half-period allowed for maximum control authority when the corrugated layer was used as an actuator. In fact, this transverse linear actuator design was patented earlier by Tibbetts [17].

Therefore, the circularly corrugated piezoelectric spring layer electrodes are etched, as shown in figure 4(a), and then woven into the form shown in figure 4(b). Note that the portions of the electrodes which are etched correspond to the undeformed centerlines of the full spring layer, $z_\mathrm{s} = 0$. The two resulting electrical biases are then combined out-of-phase to yield the maximum voltage output.

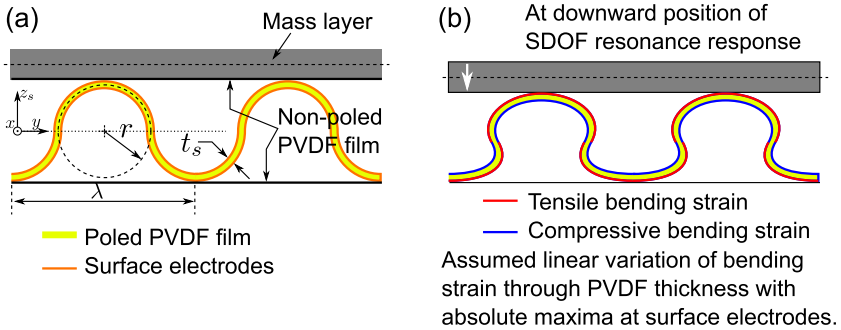

Figure 3. (a) Undeformed cross-sectional geometry of circularly corrugated piezoelectric spring layer with exaggerated electrode thickness and arbitrary top mass layer. (b) Illustrated cross-sectional response when top mass layer is displaced downward during SDOF resonant vibration. Bending strain is assumed to vary linearly through the thickness of the PVDF film.

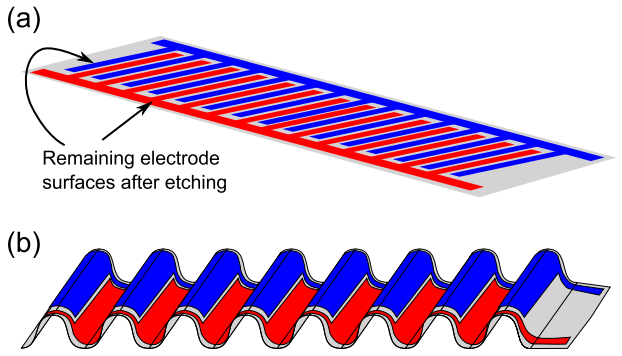

Figure 4. (a) Etching of piezoelectric material prior to corrugation and (b) the desired circularly corrugated form.

To model the electromechanical response of this form of piezoelectric spring layer, it is assumed that the electromechanical effects are induced only by the transverse displacement of the spring layer. Since the device is anticipated to exhibit a transverse SDOF resonance and energy harvesting analyses have widely shown that resonant frequencies are those which yield highest output electrical power [1, 14, 19], this is the dynamic which is most pertinent to accurately model. Furthermore, it is here assumed that the elastic transverse response of the spring layer is decoupled from the in-plane response using a superposition approach to determine the equivalent elastic stiffness components of the circularly corrugated spring [20, 21]. As a result of these assumptions, the electromechanical response is simply a one-dimensional problem related to the transverse elastic deformation of the spring layer.

3. Generalized Hamilton's principle

For the sake of conciseness, rigorous derivation of Hamilton's principle for deformable electro-elastic bodies is not here presented due to the availability of useful texts [22, 23] and a similar summary [24] elsewhere. Only unique forms of the resulting equations are hereafter explained with specific mathematical operators provided in the appendix.

For the case of a single applied piezoelectric vibration control device, there exist six unknown mechanical displacements:

$$\begin{aligned}\mathbf{u}\,(\mathbf{x},t)_\mathrm{b} &= [\,u_{\mathrm{b}o}\;\; v_{\mathrm{b}o}\;\; w_{\mathrm{b}o}]^\mathrm{T}\\ \mathbf{u}\,(\mathbf{x},t)_\mathrm{t} &= [\,u_{\mathrm{t}o}\;\; v_{\mathrm{t}o}\;\; w_{\mathrm{t}o}]^\mathrm{T}.\end{aligned} \tag{4}$$

From equation (3), the mechanical displacements of the continuous spring layer are also expressed using these unknowns. Due to the assumptions regarding the electrical characteristics of the piezoelectric material, only one unknown is required to describe this response, v_p.

The mechanical displacements are then approximated as a linear combination using the Rayleigh–Ritz method [23]:

$$\mathbf{u}\,(\mathbf{x},t)_{i=\mathrm{b,t}} = (\Psi(\mathbf{x})\mathbf{m}(t))_i \tag{5}$$

where $\Psi(\mathbf{x})$ are the admissible trial functions and $\mathbf{m}(t)$ are the generalized coordinates. The coordinate dependence may be truncated as per convention $(\mathbf{x}) = (x, y, 0) \rightarrow (x, y)$ since these displacements are defined using LK assumptions.

Substituting the approximate Ritz solutions into the generalized Hamilton's principle and assuming: that only the base plate is excited by point forces, a harmonic time dependence of the form $\exp(\mathrm{j}\omega t)$ and that the electrodes of the piezoelectric material are attached only to an external resistive load, R_1, yields a coupled system of electromechanical equations of the form

$$\begin{aligned}&\left\{\begin{bmatrix}\frac{1}{R_1} & 0 & 0\\ -\Theta_{\mathrm{s,t}} & \mathbf{K}_\mathrm{t}+\mathbf{K}_{\mathrm{s,t}} & \tilde{\mathbf{K}}_{\mathrm{s,b}}\\ -\Theta_{\mathrm{s,b}} & \tilde{\mathbf{K}}_{\mathrm{s,t}} & \mathbf{K}_\mathrm{b}+\mathbf{K}_{\mathrm{s,b}}\end{bmatrix}\right.\\ &\quad+\mathrm{j}\omega\begin{bmatrix}C_\mathrm{p} & \Theta_{\mathrm{s,t}}^\mathrm{T} & \Theta_{\mathrm{s,b}}^\mathrm{T}\\ 0 & \mathbf{C}_\mathrm{t}+\mathbf{C}_{\mathrm{s,t}} & \tilde{\mathbf{C}}_{\mathrm{s,b}}\\ 0 & \tilde{\mathbf{C}}_{\mathrm{s,t}} & \mathbf{C}_\mathrm{b}+\mathbf{C}_{\mathrm{s,b}}\end{bmatrix}\\ &\quad\left.-\omega^2\begin{bmatrix}\mathbf{0} & \mathbf{0} & \mathbf{0}\\ \mathbf{0} & \mathbf{M}_\mathrm{t}+\mathbf{M}_{\mathrm{s,t}} & \tilde{\mathbf{M}}_{\mathrm{s,b}}\\ \mathbf{0} & \tilde{\mathbf{M}}_{\mathrm{s,t}} & \mathbf{M}_\mathrm{b}+\mathbf{M}_{\mathrm{s,b}}\end{bmatrix}\right\}\begin{bmatrix}v_\mathrm{p}(\omega)\\ \mathbf{m}_\mathrm{t}(\omega)\\ \mathbf{m}_\mathrm{b}(\omega)\end{bmatrix}\\ &=\begin{bmatrix}\mathbf{0}\\ \mathbf{0}\\ \mathbf{F}(\omega)\end{bmatrix}\end{aligned} \tag{6}$$

where matrices $\mathbf{K}$, $\mathbf{C}$, $\mathbf{M}$ and Θ are the stiffness, damping, mass and electromechanical coupling terms, respectively; C_p is the capacitance of the piezoelectric film and matrices having subscript (s, i) with $i = \mathrm{b}, \mathrm{t}$ indicate components ascribed to the spring layer written in terms of the base plate, b, or the top plate, t, displacements. Those marked by $\tilde{(\,)}$ indicate elastic coupling terms due to the spring layer. All components of equation (6) are detailed in the appendix for implementation. Note that electromechanical coupling is due to the spring layer; yet, because the spring layer mechanical displacements are written in terms of the base and top plate responses, the coupling is seen to directly affect the host structural vibration as well as the response of the top mass layer of the vibration control and energy harvesting device.

In the present study, the electromechanical coupling terms are determined by

$$\Theta_{\mathrm{s,t}} = N_\mathrm{c}(h_\mathrm{s})\frac{2h_\mathrm{s}}{\pi t_\mathrm{s}}\frac{d_{31}E_z^\mathrm{s}}{h_\mathrm{s}}\int\int \Psi_{w_{\mathrm{t}o}}\,\mathrm{d}y\,\mathrm{d}x \tag{7}$$

$$\Theta_{\mathrm{s,b}} = N_\mathrm{c}(h_\mathrm{s})\frac{2h_\mathrm{s}}{\pi t_\mathrm{s}}\frac{d_{31}E_z^\mathrm{s}}{h_\mathrm{s}}\int\int -\Psi_{w_{\mathrm{b}o}}\,\mathrm{d}y\,\mathrm{d}x \tag{8}$$

where $\Psi_{w_{\mathrm{t}o}}$ and $\Psi_{w_{\mathrm{b}o}}$ are the trial functions of the top and base plate transverse displacements, respectively. Equations (7) and (8) are the result of assuming the elastic transverse displacements are decoupled from the in-plane responses and the assumption that the piezoelectric spring layer electromechanical coupling is only related to transverse displacement. These equations have further been tailored to reflect a more intuitive representation of the linear transverse strain induced in the corrugated piezoelectric film. Though

Table 1. Mechanical and electrical characteristics of the piezoelectric film.

t_s (m)	E_p (Pa)	ρ_p (kg m^{-3})	η	d_{31} (m V^{-1})	ϵ_{33}^T (F m^{-1})
28×10^{-6}	5.4×10^9	1780	1×10^{-3}	23×10^{-12}	$12\epsilon_0$

the spring layer is deformed transversely, the piezoelectric coefficient d_{31} related to bending is employed, as opposed to d_{33}, which is related to through-thickness deformation. Secondly, a weighting term is applied, $N_c \frac{2h_s}{\pi t_s}$, which is the product of the number of corrugations, N_c, and the ratio of the equivalent continuous area of the spring layer to the actual corrugated cross-sectional area. These modifications have been made following empirical observation of the devices' electrical response in the laboratory but in fact reflect an intuitive connection to the bending strain of the corrugated spring as it is transversely deformed.

The frequency response function (FRF) of the top plate transverse acceleration to the base plate transverse acceleration is computed as

$$|\mathrm{FRF}_{\mathrm{accel}}(\omega)| = \left| \frac{-\omega^2 w_{to}(x_1, y_1, \omega)}{-\omega^2 w_{bo}(x_2, y_2, \omega)} \right| = \left| \frac{\Psi_{w_{to}}(x_1, y_1)\mathbf{m}_{w_{to}}(\omega)}{\Psi_{w_{bo}}(x_2, y_2)\mathbf{m}_{w_{bo}}(\omega)} \right| \quad (9)$$

where $\mathbf{m}_{w_{to}}$ are the generalized coordinates related to the top plate transverse displacement, $\mathbf{m}_{w_{bo}}$ are the generalized coordinates related to the base plate transverse displacement, and (x_1, y_1) and (x_2, y_2) are the points of evaluation. The voltage FRF (V g^{-1}) of a device is computed as

$$|\mathrm{FRF}_{\mathrm{volt}}(\omega)| = \left| \frac{v_p(\omega)}{-\omega^2 \Psi_{w_{bo}}(x_2, y_2)\mathbf{m}_{w_{bo}}(\omega)} \right| \quad (10)$$

where the peak voltage across the electrodes $v_p(\omega)$ from equation (6) is employed.

The accelerance is the transfer function between the panel acceleration and the input force. In experiments, the spatial average of the panel acceleration is computed as the square root of the ensemble average of the individual acceleration measurements squared. The accelerance is thereafter the ratio of this value to the driving force. In modeling, the accelerance is integrated over the panel surface:

$$\frac{\ddot{w}_{bo}(\omega)}{\mathbf{F}(\omega)} = \frac{1}{\mathbf{F}(\omega)} \left[\frac{\omega^4}{2a_b b_b} \int\int \left(\Psi_{w_{bo}}(x, y)\mathbf{m}_{w_{bo}}(\omega)\right)^* \times \left(\Psi_{w_{bo}}(x, y)\mathbf{m}_{w_{bo}}(\omega)\right) \mathrm{d}x\,\mathrm{d}y \right]^{1/2}. \quad (11)$$

Average electrical power over the energy harvesting load resistance is computed:

$$P(\omega) = \frac{|v_p(\omega)|^2}{2R_1}. \quad (12)$$

When the device is placed on the host panel, similar to the accelerance TF, the power TF is the ratio of the electrical power to the input force.

Table 2. Equivalent orthotropic plate characteristics of piezoelectric core having $\lambda = 12.7$ mm.

E_x (Pa)	E_y (Pa)	E_x (Pa)	ν_{yx}	ν_{yz}	ν_{xz}
2.47×10^{10}	2.12×10^{10}	5.78×10^3	0.045	0	0
G_{yz} (Pa)	G_{xz} (Pa)	G_{xy} (Pa)	ρ_s (kg m^{-3})	h_s (mm)	η_s
7.49×10^4	1.77×10^6	2.69×10^8	7.12	6.35	0.08

4. Model validation: shaker test

4.1. Device description and characterization

The device shown in figure 2 was produced using a piezoelectric film having characteristics as given in table 1 [25]. Both surface electrodes were carefully etched as per the design of figure 4 using a fine-tipped watercolor brush and ferric chloride solution. Afterwards, the film was constrained using thin lines of quick-drying epoxy and facing sheets of non-poled PVDF film into the circularly corrugated form having five full periods. Evident in figure 2 are the lead attachments connected to the etched surface electrodes, noting that four connections are required given the four unique segments of the electrode after etching. Elastic homogenization techniques were used to determine equivalent orthotropic thick plate elasticity parameters to characterize the spring layer stiffness matrix, $\mathbf{c}_s^E$ [20, 26, 27]. These equivalent material properties are given in table 2. Note that the transverse parameter, E_z, is many orders of magnitude less than the cross-planar bending stiffnesses, E_x and E_y, and that there is no coupling between them, $\nu_{yz} = \nu_{xz} = 0$. This indicates that transverse dynamics of the layer are similar to a layer of vertical springs, as per [20], not coupled to the remaining dynamics of the layer.

The device was fixed to a stiff shaker table platform for FRF testing. A diagram of the test is provided in figure 5. A Polytec OFV 501 laser vibrometer and OFV 2600 controller measured the transverse velocity of the device top mass, whereafter acceleration was approximated by assuming harmonic time dependence: $\ddot{w}_{to} = \mathrm{j}\omega\dot{w}_{to}$. Table 3 presents the top mass layer and approximate base plate characteristics. The shaker excited the table with white noise bandpass filtered from 50 to 400 Hz and a table-mounted PCB 352A10 accelerometer served as reference of the input excitation. The drive acceleration used during the test was 14.2 m s^{-2} (1.45 g). In the model, the base plate was assumed to have free boundary conditions and be excited by a centrally located unit point force. For FRF computation, $(x_1, y_1) = (0, 0)$ and $(x_2, y_2) = (0, 0)$.

Table 3. Mechanical and geometric properties of base and top plates, $i = \text{b, t}$.

Layer	a_i (mm)	b_i (mm)	h_i (mm)	E_i (Pa)	ν_i	ρ_i (kg m^{-3})	η_i
Base	300	140	5	1.0×10^{14}	0.33	800	3×10^{-4}
Mass layer	76.2	50.8	0.76	2.1×10^{11}	0.33	7850	1×10^{-3}

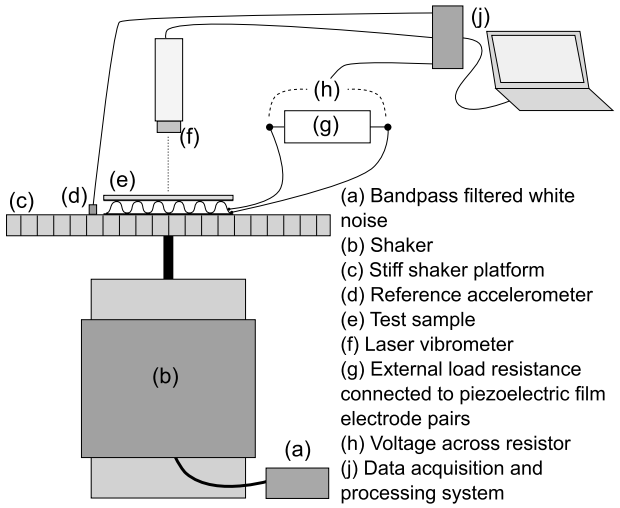

Figure 5. Experimental FRF test schematic used for model validation.

4.2. FRF test results and model validation

A comparison of the measured and modeled acceleration FRF is given in figure 6(a) for four values of load resistance, R_1. The device is observed to exhibit a principal SDOF resonance, akin to a 1D mass–spring–damper system. For smaller values of R_1, the natural frequency occurs at approximately 78.5 Hz; as the resistance is increased, the coupling through the piezoelectric material produces a stiffer distributed spring layer and increases the resonance to the open circuit value (i.e. $R_1 \to \infty$) at approximately 81.5 Hz. This is a substantial shift in frequency for a piezoelectric material having such low electromechanical coupling as compared with, for example, piezoceramics. However, this may be due to the circularly corrugated design which induces relatively high bending strain in the film as the mass oscillates vertically at resonance. The model almost exactly predicts the locations of these resonant frequencies for various load resistances but measurements exhibited uniformly more roll-off above resonance. This lapse in the model may be explained by employing too great of a loss factor, η_s, in table 2, for the equivalent spring layer elastic material properties.

It is also noted that there is no noticeable shunt damping effect due to dissipation in the electrical circuit. The inertial influence of the top mass layer dominates dissipative circuit effects. Therefore, for this particular specimen the damping of the device is mostly a function of the elastic characteristics of the PVDF film itself as opposed to electromechanical coupling.

Figure 6(b) compares the measured and predicted voltage FRF for the sample. The model fairly accurately predicts the amplitude and shifting resonance frequency of the voltage FRF resonance. Similar to past work in piezoelectric energy harvesting [14], the voltage FRF is measured and predicted to both increase in overall amplitude as well as in frequency as the load resistance of the energy harvesting circuit is increased.

Finally, a time-domain plot of the response of the device as measured for $R_1 = 150$ kΩ is given in figure 7 at an excitation frequency of 81 Hz and drive acceleration also of 14.2 m s^{-2} (1.45 g). Shown in figure 7(a) are the individual voltage outputs for the two electrode pairs generated by etching according to the design in figure 4. The outputs are perfectly out-of-phase and of nearly identical magnitude. This verifies the assumption that the strains exhibited on opposing sides of the piezoelectric film are equal and opposite. Proper

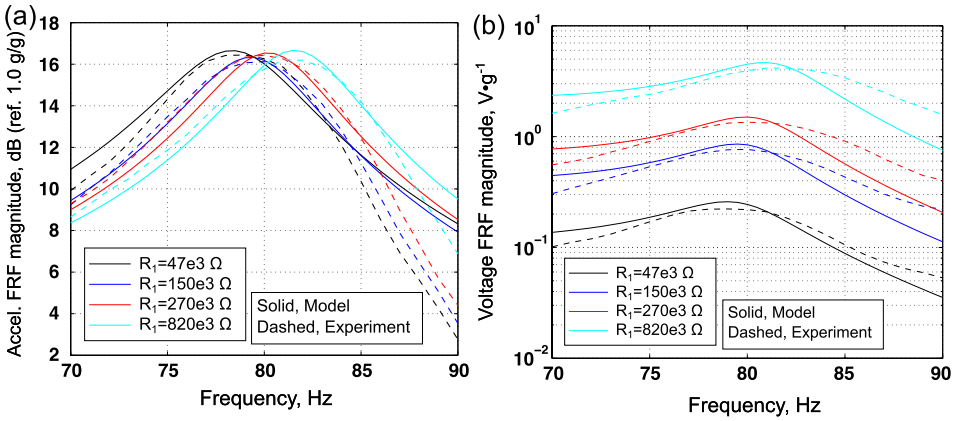

Figure 6. Comparison of modeled and measured (a) acceleration FRF magnitudes and (b) voltage FRF magnitudes for piezoelectric corrugated core distributed absorber device for various load resistances, R_1.

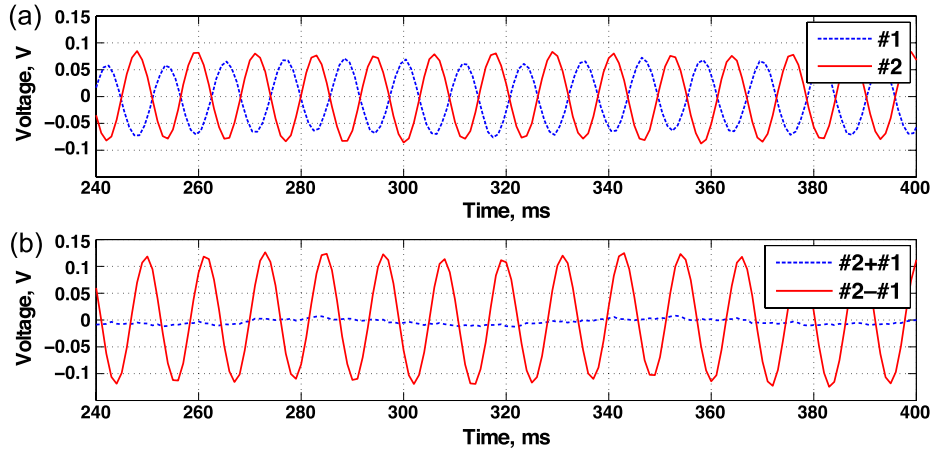

Figure 7. Measured time series of corrugated piezoelectric device. (a) Individual electrode outputs and (b) sum and difference of the two signals.

Table 4. Mechanical and geometric properties of base and top plates, $i = \text{b, t}$.

Layer	a_i (mm)	b_i (mm)	h_i (mm)	E_i (Pa)	ν_i	ρ_i (kg m^{-3})	η_i
Base	711	508	6.35	7.2×10^{10}	0.33	2100	1×10^{-3}
Mass layer	150	150	1.3	7.2×10^{10}	0.33	2100	1×10^{-3}

combination of these voltages yields a substantial increase in output, while directly combining the two signals almost eliminates the net voltage, figure 7(b).

The response is also observed to be sinusoidal, indicating the linearity of the distributed spring layer as the device transversely oscillates. This is a beneficial finding given that one might assume the bending strain induced in the corrugated spring is substantial for the present amplitude of exciting acceleration of 14.2 m s^{-2} (1.45 g). However, in practice, little displacement from the undeformed configuration is observed as the device oscillates on the shaker. This may be explained by the fact that the transverse force of the mass deflecting the corrugated spring is distributed over a broader surface as compared to a point vibration absorber which generally deflects its spring to a much greater degree.

While no sensitivity analysis is here performed to determine at what level of input vibration the induced bending strain in the corrugated spring begins to exhibit nonlinear characteristics, the amplitude of vibration presently measured in shaker testing is sufficiently great to assume most realistic scenarios would also exhibit linear elastic and electrical response (a number of realistic ambient vibration acceleration levels are detailed in [28–30] and often have a magnitude less than 1 g). The linearity of the transverse response suggests model results for the device at its natural frequency should be in reasonable agreement with measurements which is most important for energy harvesting analyses.

5. Panel experiment description

A simply supported panel was then used for testing another piezoelectric vibration control device. The panel itself was a part of a larger mounted structure with the panel extending off of the structure by means of thin shims to replicate simple supports as closely as possible. The mechanical and geometric information of the panel and the device top mass layer are provided in table 4. It was observed that the edges of the panel support were not exactly classical simple supports but additionally constrained the rotation of the edges. This was compensated for in the modeling by including additional edge stiffnesses in computation. This is achieved by assuming the edge is further constrained by rotational springs as described in [31] and [32]. However, due to the inexact boundaries along the edges of the test panel, it was not possible to perfectly match eigenfrequency predictions of the panel with those measured.

The mounted structure and the panel were both suspended as shown in figure 8 with a test schematic shown in figure 9. An electrodynamic shaker was attached to a bored hole at the center of the panel through a short stinger. The shaker input was bandpass-filtered white noise from 50 to 800 Hz. A PCB 208 A03 force transducer was positioned between the stinger and the panel. An array of 30 PCB 330A accelerometers were randomly positioned on the underside of the panel, with the top surface left clear for later application of the piezoelectric device. The global accelerance TF was computed as the square root of the ensemble average of the squared accelerance TFs between each accelerometer and the force transducer.

The piezoelectric spring layer design was the same as for the earlier sample, having piezoelectric film characteristics as given in table 1 and equivalent elastic parameters as provided in table 2. A close-up photograph of the device attached to the panel is shown in figure 10. The device was much larger than the specimen used in FRF testing of section 4 and included 12 periods of the circular corrugation. However, despite the larger size, the mass ratio of the device relative to the mass of

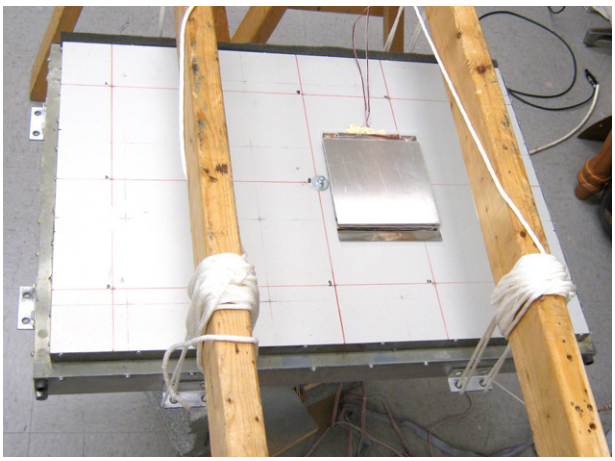

Figure 8. Photograph of simply supported panel in mounted structure with piezoelectric device attached to the top surface. The shaker, stinger, force transducer and accelerometer array are connected to the underside of the panel from the photograph perspective.

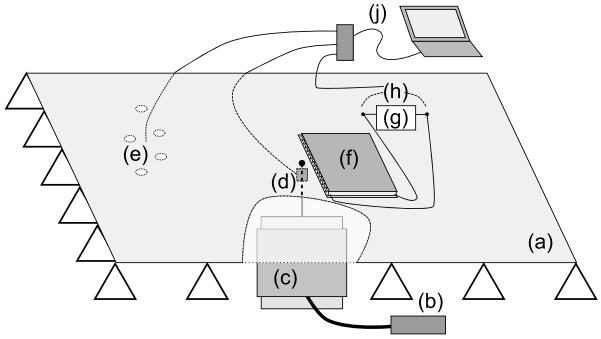

Figure 9. Panel test set-up schematic: (a) panel; (b) bandpass-filtered white noise; (c) shaker; (d) force transducer; (e) accelerometer array distributed over the full bottom surface of panel; (f) piezoelectric device attached to top panel surface; (g) external load resistance; (h) voltage across resistor; (j) data acquisition and processing system.

the panel was only $\mu = 0.0104$, or just over 1%. In practical terms, this is an unusually lightweight device to employ for vibration control purposes but also meets the general objective in energy harvesting of attaching devices of negligible inertial influence to the host structure. Though the device was not measured on the shaker platform, for the justified reason that removing such devices from the platform often resulted in the destruction of the piezoelectric film layer, the SDOF natural frequency of the device was predicted by the model to be approximately 94 Hz. This was very close to the (1, 1) mode of the simply supported panel which was measured and computed to be 97.5 Hz.

6. Panel experimental results and model comparison

The panel accelerance TF was initially measured with nothing attached to the top surface. Afterwards, the center of the piezoelectric device was attached at (93, 0) mm relative to the panel center. The device was attached by means of

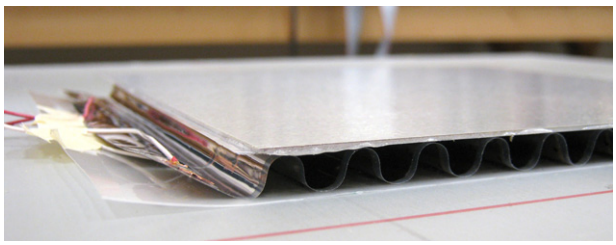

Figure 10. Photograph of the piezoelectric vibration control device attached to the panel.

a thin double-sided tape. The tests were repeated varying the load resistance, R_1, in the energy harvesting circuit to which the electrical leads from the etched electrodes were attached. The out-of-phase voltages from the electrodes were appropriately combined so as to yield the maximum electrical signal. The untreated panel accelerance TF and that with the applied piezoelectric device are shown in figure 11 comparing predicted results and measurements when the external resistance was $R_1 = 180\ \text{k}\Omega$.

The model very closely predicts the untreated panel response with the exception of the location of some resonances. This is attributed to the inexact simply supported boundary conditions of the panel. It is apparent that the connection of the shaker to the panel is not exactly at the panel center since several of the asymmetric modes are excited, for instance the (2, 1) mode at 186 Hz. After observation of this feature, the model was appropriately adjusted to simulate the point force excitation at (4, 4) mm relative to the panel center. The two lowest-order symmetric panel resonances—the (1, 1) mode at 97.5 Hz and the (3, 1) mode at 350 Hz—are thoroughly excited by the shaker and these are the resonances for which the piezoelectric device was designed and appropriately positioned. This is illustrated in figure 12 showing the device placed near to the anti-nodes of the (1, 1) and (3, 1) modes. The ideal position for attenuating these modes was to place the device at the panel center but this was not achievable due to interference from the shaker connection.

Following application of the device, the panel vibration of the (1, 1) mode is observed to be significantly attenuated. The resonance at 97.5 Hz is predicted to be suppressed by approximately 20 dB and the measurements show a similar amplitude of attenuation. Two split resonances at 87 and 100 Hz are generated by application of the reactive device. This is a dynamic ascribed to conventional 1D vibration absorbers [33] and is seen to also be the case for the distributed system of interest. This further exemplifies the reactive nature of the piezoelectric device in suppressing the panel response. The (3, 1) panel resonance at 350 Hz is attenuated by more than 10 dB but this is not due to the direct 'tuning' of the device for this frequency. Instead, the reactive suppression of the symmetric (3, 1) mode is conveniently achieved by the mostly central placement of the device on the panel surface. Over the bandwidth of frequencies computed, the model is in very close agreement with the measurements, despite minor misalignment of panel resonances due to the inexact simple supports.

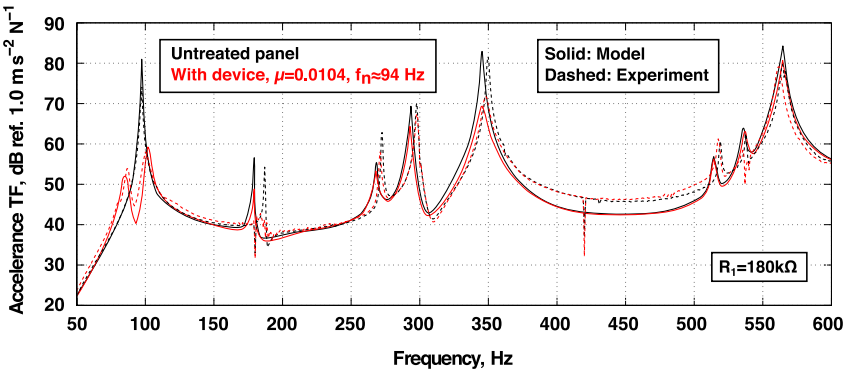

Figure 11. Comparison of modeled (solid curves) and measured (dashed curves) accelerance TF magnitudes of the panel when untreated (black plots) and with the piezoelectric device (red plots). $R_1 = 180$ kΩ.

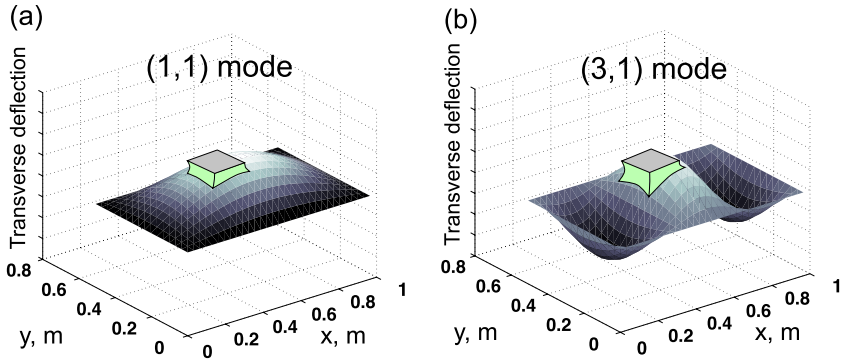

Figure 12. Illustration of positioning of device on panel to attenuate (a) (1, 1) mode and (b) (3, 1) mode. Spring layer shown as a continuum, as in figure 1, with exaggerated deformation of panel and device spring layer for ease of visualization.

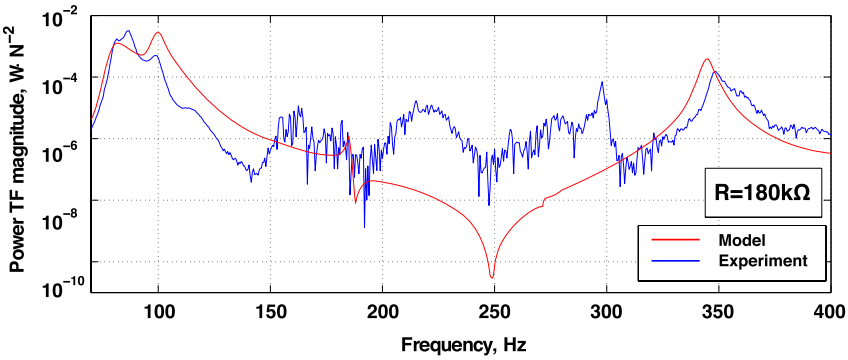

Figure 13. Comparison of modeled and measured electrical power TF magnitude of the piezoelectric device. $R_1 = 180$ kΩ.

While the device is observed to dramatically suppress the panel vibration for being such a lightweight treatment, the second objective pursued is the achievement of useful electrical power output from the device. For a load resistance of $R_1 = 180$ kΩ, the power TF magnitude is shown in figure 13. For the two symmetric modes in this bandwidth—(1, 1) at 97.5 Hz and (3, 1) at 350 Hz—the measurements show very clear maxima in the electrical power response. While the model is close in replicating the magnitude of the power around the device SDOF natural frequency, 94 Hz, it slightly under-estimates the peak response which it predicts to occur at 100 Hz, the higher of the two split resonances.

Measurements at 86.5 Hz observed a maximum power TF magnitude of 3.3 mW N^{-2}. The power TF is not easily compatible with other metrics in the energy harvesting literature, more often quoted as power FRFs with units W g^{-2} or simply as power at a given exciting acceleration level. Thus, the panel was instead excited only at 86.5 Hz. The measured average electrical power was then 0.441 μW (peak voltage of 0.3986 V) while the drive acceleration at the panel center (shaker attachment) was measured to be 3.29 m s^{-2} (0.335 g). This low amplitude of measured power also suggests the film is strained within a linear range given another study in the literature which employed piezoelectric film and achieved power levels of the order of mW [34].

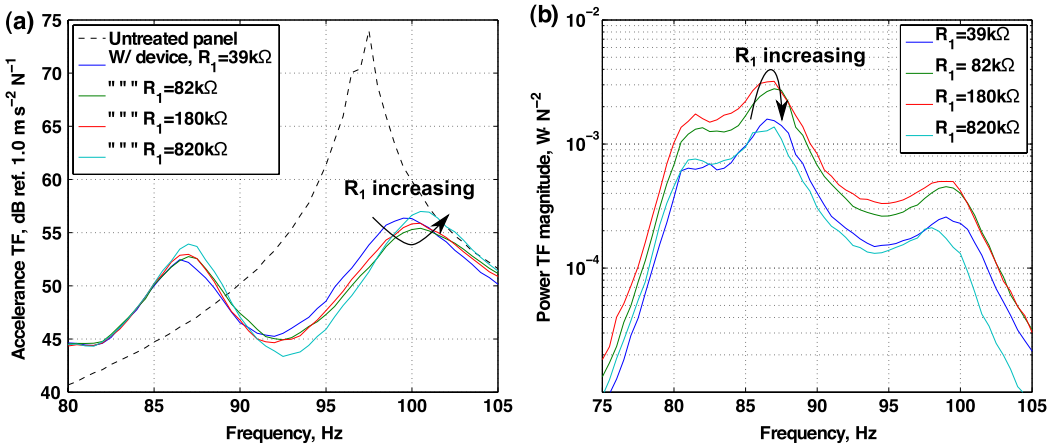

Figure 14. (a) Panel acceleration TF around (1, 1) mode and (b) piezoelectric device power TF for a variety of resistances R_1.

Figure 13(b) also shows that electrical response for the device when excited by panel asymmetric modes yielded stray electrical signals, and thus the noisy response observed between 120 and 320 Hz. The model does not take into account the precise geometry of the circularly corrugated spring layer and, instead, predicts a precipitous electrical signal drop in this bandwidth, greater than seven orders of magnitude. Since it is not feasible to measure such a range in electrical response, the measured noisy electrical output is understandable.

Figure 14(a) plots the measured panel response around the (1, 1) mode for a variety of load resistances, R_1. Changing the load resistance is here observed to influence the magnitude of the vibration suppression around the (1, 1) mode. This suggests that the larger piezoelectric vibration control device, in contrast to the much smaller sample used in FRF testing, exhibits enough electromechanical coupling through the many piezoelectric corrugations to take advantage of shunt damping effects in the energy harvesting circuit.

What is perhaps more interesting, however, is the effect on the panel response measured for the higher of the two split resonances, at 100 Hz. For low R_1, this resonance occurs at 99 Hz. Increasing load resistance dampens this resonance and increases the frequency to 100 Hz. Further increasing R_1 reduces the damping effect and increases the resonance up to 101 Hz. A load resistance of $R_1 = 82$ kΩ yields an additional 2 dB of vibration attenuation of the 100 Hz split resonance as compared with open circuit conditions, $R_1 = \rightarrow \infty$. This emulates the piezoelectric shunt damping effects characteristic of other more frequently studied systems like cantilevered piezoelectric beams [9]. This also further verifies the analogy between the present energy harvesting device and an electromechanically stiffened and damped vibration absorber.

Figure 14(b) plots the measured device power TF for the same selections of load resistance. The maximum power TF achieved from these resistances occurs for $R_1 = 180$ kΩ: 3.3 mW N^{-2} at 86.5 Hz. Smaller or greater load resistances yield reduced maximum output. It is also noted that both objectives are best met by nearly the same choice of R_1: vibration suppression of the panel is best achieved using $R_1 =$ 82 kΩ while energy harvesting objectives maximize power for $R_1 \approx 180$ kΩ. For low to moderately electromechanically coupled piezoelectric harvesters, this has elsewhere been observed in the literature with regards to damping of the harvester itself [7, 14, 19].

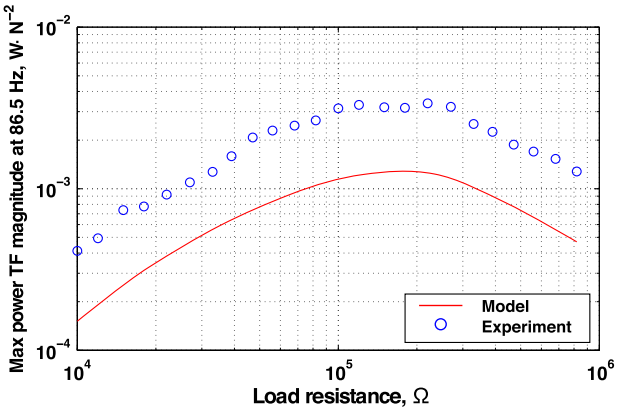

Figure 15. Comparison of modeled and measured electrical power TF magnitude of the piezoelectric device at 86.5 Hz for various R_1.

Figure 15 plots the power TF magnitude at 86.5 Hz for various load resistances. Modeled results are uniformly less than those measured. As observed in figure 12, this disparity is explained by the fact that the model predicts the maxima to occur at 100 Hz instead of 86.5 Hz. However, the trend between the two plots is similar and shows a clear optimum range of load resistance for maximizing electrical power output. As previously observed, this range also corresponds roughly to the same selection of R_1 that best suppresses panel vibration.

Compared to the power TF which appears promising given the order of mW, the actually observed maximum average power (0.441 μW for panel center drive acceleration of 3.29 m s^{-2}) falls well within or below the range of many other piezoelectric energy harvesters in the literature [30, 35]. This indicates there is a need for an improved metric of achievable power in the event the host structure may be dynamically influenced by the attached harvesting device. The power TF has already been employed elsewhere in

the literature in a non-dimensional form when the main structure and attached harvester are both lumped parameter systems [11]. This is a more suitable use for the power TF given the direct relation between applied force, the system mass and the resulting acceleration. In contrast, distributed systems like the present plate are characterized by governing equations of greater complexity, which suggests an improved metric of generated power due to an applied force or system acceleration should be proposed. At present, a more direct metric—measured average power when the panel is driven at a single frequency—appears sufficient for immediate comparison against other harvester designs.

7. Conclusions

This paper presented a model based on the generalized Hamilton's principle to approximate the coupled electro-elastic response of a host structure and attached distributed piezoelectric vibration control devices. The purpose of the model is to estimate the benefit of such devices in achieving two objectives: (i) vibration suppression of the panel via reactive and resistive dynamics and (ii) energy harvesting through deformation of the piezoelectric spring layer and coupling to an external circuit. While the electromechanical influences on energy harvesters themselves have been widely studied and reported, this analysis focuses on the influence of the harvester on the exciting host structure. In this perspective, the harvesters are analogous to electromechanically stiffened and damped vibration absorbers.

One such device design was considered in detail. These devices used a distributed spring layer constructed from a circularly corrugated piezoelectric film having electrodes appropriately etched to maximize the voltage output. One sample was attached to a shaker table to measure acceleration and voltage FRFs which were compared against model predictions. The model was found to be in close agreement regarding the location of the SDOF natural frequency of the device and also accurately replicated the effects of electromechanical coupling through the piezoelectric spring layer as the external load resistance was modified.

A larger piezoelectric device was then manufactured and applied to a lightly damped structural panel which was excited by random vibration. The added device represented roughly a 1% addition of mass to the host structure and was designed so as to reactively suppress the (1, 1) mode of the panel. The addition of the device was seen to significantly suppress this resonance, akin to classical vibration absorbers, and the electromechanical coupling effects due to shunt damping were observed to further suppress the panel vibration by changing the stiffness and damping characteristics of the spring layer as the electrical load resistance was modified. The electrical power TF was maximized when the load resistance was slightly greater than that corresponding to the choice which most suppressed the panel vibration. This indicates both objectives may be nearly achieved simultaneously for the piezoelectric vibration control device considered.

Acknowledgments

The author is grateful for the continued encouragement of Kevin Smith of Newport News Shipbuilding. The author would also like to thank the reviewers for valuable comments.

Appendix. Components of equation (6)

$$\mathbf{K} = \sum_{i=\mathrm{b,s,t}} \int_{V_i} (\mathbf{L_u}\Psi(\mathbf{x}))_i^{\mathrm{T}}\, \mathbf{c}_i^{\mathrm{E}}\, (\mathbf{L_u}\Psi(\mathbf{x}))_i \,\mathrm{d}V_i \tag{A.1}$$

$$\mathbf{M} = \sum_{i=\mathrm{b,s,t}} \rho_i \int_{V_i} (\Psi^{\mathrm{T}}(\mathbf{x}))_i\, (\Psi(\mathbf{x}))_i \,\mathrm{d}V_i \tag{A.2}$$

$$\mathbf{C} = \alpha\mathbf{M} + \beta\mathbf{K}. \tag{A.3}$$

Here, $\alpha = 0$ and $\beta = \eta/\omega$ to employ loss factor damping:

$$\mathbf{F} = [\Psi^{\mathrm{T}}(\mathbf{x}_{f_1}) \cdots \Psi^{\mathrm{T}}(\mathbf{x}_{f_{N_f}})]. \tag{A.4}$$

The linear differential operator for the Love–Kirchhoff plates is

$$(\mathbf{L_u})_{i=\mathrm{b,t}} = \begin{bmatrix} \dfrac{\partial}{\partial x} & 0 & 0 \\ 0 & \dfrac{\partial}{\partial y} & 0 \\ \dfrac{\partial}{\partial y} & \dfrac{\partial}{\partial x} & 0 \end{bmatrix}. \tag{A.5}$$

The linear differential operator for the thick orthotropic plate is

$$(\mathbf{L_u})_{\mathrm{s}} = \begin{bmatrix} \dfrac{\partial}{\partial x} & 0 & 0 \\ 0 & \dfrac{\partial}{\partial y} & 0 \\ 0 & 0 & \dfrac{\partial}{\partial z_{\mathrm{s}}} \\ 0 & \dfrac{\partial}{\partial z_{\mathrm{s}}} & \dfrac{\partial}{\partial y} \\ \dfrac{\partial}{\partial z_{\mathrm{s}}} & 0 & \dfrac{\partial}{\partial x} \\ \dfrac{\partial}{\partial y} & \dfrac{\partial}{\partial x} & 0 \end{bmatrix}. \tag{A.6}$$

The stiffness matrices of the Love–Kirchhoff plates are

$$\mathbf{c}_{i=\mathrm{b,t}}^{\mathrm{E}} = \begin{bmatrix} \dfrac{E_i}{1-\nu_i^2} & \dfrac{\nu_i E_i}{1-\nu_i^2} & 0 \\ \dfrac{\nu_i E_i}{1-\nu_i^2} & \dfrac{E_i}{1-\nu_i^2} & 0 \\ 0 & 0 & \dfrac{E_i}{2(1+\nu_i)} \end{bmatrix}. \tag{A.7}$$

For the thick orthotropic plate the stiffness matrix is expressed as

$$\mathbf{c}_{\mathrm{s}}^{\mathrm{E}} = \begin{bmatrix} \frac{1}{E_x} & -\frac{\nu_{yx}}{E_y} & -\frac{\nu_{zx}}{E_z} & 0 & 0 & 0 \\ -\frac{\nu_{xy}}{E_x} & \frac{1}{E_y} & -\frac{\nu_{zy}}{E_z} & 0 & 0 & 0 \\ -\frac{\nu_{xz}}{E_x} & -\frac{\nu_{yz}}{E_y} & \frac{1}{E_z} & 0 & 0 & 0 \\ 0 & 0 & 0 & \frac{1}{G_{yz}} & 0 & 0 \\ 0 & 0 & 0 & 0 & \frac{1}{G_{xz}} & 0 \\ 0 & 0 & 0 & 0 & 0 & \frac{1}{G_{xy}} \end{bmatrix}^{-1}. \quad \text{(A.8)}$$

The capacitance of the piezoelectric layer, $C_{\mathrm{p}} = [A_{\mathrm{p}}(\epsilon_{33}^{\mathrm{T}} - d_{31}^2 E_{\mathrm{p}})]/t_s$, is a function of: A_{p}, the area of the electrodes; $\epsilon_{33}^{\mathrm{T}}$, the permittivity matrix component evaluated at constant stress; d_{31}, the piezoelectric constant; E_{p}, the Young's modulus of the piezoelectric material; and t_{s}, the thickness of the piezoelectric material.

References

[1] Poulin G, Sarraute E and Costa F 2004 Generation of electrical energy for portable devices comparative study of an electromagnetic and piezoelectric system *Sensors Actuators* A **116** 461–71

[2] Beeby S P, Tudor M J and White N M 2006 Energy harvesting vibration sources for microsystems applications *Meas. Sci. Technol.* **17** R175–95

[3] Stephen N G 2006 On energy harvesting from ambient vibration *J. Sound Vib.* **293** 409–25

[4] Elvin N G, Lajnef N and Elvin A A 2006 Feasibility of structural monitoring with vibration powered sensors *Smart Mater. Struct.* **15** 977–86

[5] Erturk A 2011 Piezoelectric energy harvesting for civil infrastructure system applications: moving loads and surface strain fluctuations *J. Intell. Mater. Syst. Struct.* **17** 1959–73

[6] Liu J Q *et al* 2008 A MEMS-based piezoelectric power generator array for vibration energy harvesting *Microelectron. J.* **39** 802–6

[7] Lesieutre G A, Ottman G K and Hofmann H F 2004 Damping as a result of piezoelectric energy harvesting *J. Sound Vib.* **269** 991–1001

[8] Sodano H A, Park G and Inman D J 2004 Estimation of electric charge output for piezoelectric energy harvesting *Strain* **40** 49–58

[9] Karami M A and Inman D J 2011 Equivalent damping and frequency change for linear and nonlinear hybrid vibrational energy harvesting systems *J. Sound Vib.* **330** 5583–97

[10] De Marqui Junior C, Erturk A and Inman D J 2010 Piezoaeroelastic modeling and analysis of a generator wing with continuous and segmented electrodes *J. Intell. Mater. Syst. Struct.* **21** 983–93

[11] Tang X and Zuo L 2011 Enhanced vibration energy harvesting using dual-mass systems *J. Sound Vib.* **330** 5199–209

[12] Cassidy I L, Scruggs J T, Behrens S and Gavin H P 2011 Design and experimental characterization of an electromagnetic transducer for large-scale vibratory energy harvesting applications *J. Intell. Mater. Syst. Struct.* **22** 2009–24

[13] Lu F, Lee H P and Lim S P 2004 Modeling and analysis of micro piezoelectric power generators for micro-electromechanical-systems applications *Smart Mater. Struct.* **13** 57

[14] Erturk A and Inman D J 2009 An experimentally validated bimorph cantilever model for piezoelectric energy harvesting from base excitations *Smart Mater. Struct.* **18** 025009

[15] Jacquot R G and Foster J E 1977 Optimal cantilever dynamic vibration absorbers *J. Eng. Indust.* **99** 138–41

[16] Fuller C R and Cambou P 1998 An active–passive distributed vibration absorber for vibration and sound radiation control *J. Acoust. Soc. Am.* **104** 1851

[17] Tibbetts G C 1977 Transducer having piezoelectric film arranged with alternating curvatures *US Patent* #4,056,742

[18] Gentry-Grace C A 1998 A study of smart foam for noise control applications *PhD Thesis* Virginia Polytechnic Institute and State University, Blacksburg, Virginia

[19] Liao Y and Sodano H A 2009 Structural effects and energy conversion efficiency of power harvesting *J. Intell. Mater. Syst. Struct.* **20** 505–14

[20] Frostig Y and Baruch M 1990 Bending of sandwich beams with transversely flexible core *AIAA J.* **28** 523–31

[21] Harne R L and Fuller C R 2011 Modeling of a passive distributed vibration control device using a superposition technique *J. Sound Vib.* **331** 1859–69

[22] Meirovitch L 1967 *Analytical Methods in Vibrations* (New York: Macmillan)

[23] Reddy J N 1984 *Energy and Variational Methods in Applied Mechanics: With An Introduction to the Finite Element Method* (New York: Wiley)

[24] De Marqui Junior C, Erturk A and Inman D J 2009 An electromechanical finite element model for piezoelectric energy harvester plates *J. Sound Vib.* **327** 9–25

[25] Bailo K C, Brei D E and Grosh K 2003 Investigation of curved polymeric piezoelectric active diaphragms *J. Vib. Acoust.* **125** 145–54

[26] Libove C and Hubka R E 1951 Elastic constants for corrugated-core sandwich plates *Technical Note 2289* National Advisory Committee for Aeronautics

[27] Cheng Q H, Lee H P and Lu C 2006 A numerical analysis approach for evaluating elastic constants of sandwich structures with various cores *Compos. Struct.* **74** 226–36

[28] Roundy S 2005 On the effectiveness of vibration-based energy harvesting *J. Intell. Mater. Syst. Struct.* **16** 809–23

[29] Reilly E K, Miller L, Fain R and Wright P K 2009 A study of ambient vibrations for piezoelectric energy scavenging *POWERMEMS: Int. Workshop on Micro and Nanotechnology for Power Generation and Energy Conversion Applications (Washington, DC)* pp 312–5

[30] duToit N E, Wardle B L and Kim S G 2005 Design considerations for MEMS-scale piezoelectric mechanical vibration energy harvesters *Integr. Ferroelectr.* **71** 121–60

[31] Carmichael T E 1959 The vibration of a rectangular plate with edges elastically restrained against rotation *Q. J. Mech. Appl. Math.* **12** 29–42

[32] Dozio L 2011 On the use of the trigonometric Ritz method for general vibration analysis of rectangular Kirchhoff plates *Thin-Walled Struct.* **49** 129–44

[33] Den Hartog J P 1985 *Mechanical Vibrations* 4th edn (New York: Dover) pp 87–100

[34] Granstrom J, Feenstra J, Sodano H A and Farinholt K 2007 Energy harvesting from a backpack instrumented with piezoelectric shoulder straps *Smart Mater. Struct.* **16** 1810–20

[35] Cook-Chennault K A, Thambi N and Sastry A M 2008 Powering MEMS portable devices—a review of non-regenerative and regenerative power supply systems with special emphasis on piezoelectric energy harvesting systems *Smart Mater. Struct.* **17** 043001